

Journal of Materials Chemistry A

Accepted Manuscript



This is an *Accepted Manuscript*, which has been through the Royal Society of Chemistry peer review process and has been accepted for publication.

Accepted Manuscripts are published online shortly after acceptance, before technical editing, formatting and proof reading. Using this free service, authors can make their results available to the community, in citable form, before we publish the edited article. We will replace this *Accepted Manuscript* with the edited and formatted *Advance Article* as soon as it is available.

You can find more information about *Accepted Manuscripts* in the [Information for Authors](#).

Please note that technical editing may introduce minor changes to the text and/or graphics, which may alter content. The journal's standard [Terms & Conditions](#) and the [Ethical guidelines](#) still apply. In no event shall the Royal Society of Chemistry be held responsible for any errors or omissions in this *Accepted Manuscript* or any consequences arising from the use of any information it contains.

Piezoelectric Properties of CH₃NH₃PbI₃ Perovskite Thin Films and Applications for Piezoelectric Generators

Yun-Jeong Kim,¹ Tran-Van Dang,¹ Hyung-Jin Choi,¹ Byeong-Ju Park,¹ Ji-Ho Eom,¹ Hyun-A Song,² Daehee Seol,³ Yunseok Kim,³ Sung-Ho Shin,⁴ Junghyo Nah,^{4,*} and Soon-Gil Yoon^{1,*}

¹Department of Materials Science and Engineering, Chungnam National University, Daeduk Science Town, 34134, Daejeon, Korea

²Research Analysis Center, Korea Advanced Institute of Science and Technology, 291 Daehak-ro, Yuseong-gu, 34134, Daejeon, Korea

³School of Advanced Materials Science and Engineering, Sungkyunkwan University (SKKU), Suwon, 16419, Korea

⁴Department of Electrical Engineering, Chungnam National University, Daeduk Science Town, 34134, Daejeon, Korea

*Corresponding author: sgyoon@cnu.ac.kr, jnah@cnu.ac.kr

Abstract

CH₃NH₃PbI₃ (MAPbI₃) perovskite thin films were applied to fluorine-doped SnO₂ (FTO)/glass and Au/Ti/polyethylene terephthalate (PET) substrates via a two-step process, which involved depositing a CH₃NH₃I (MAI) solution onto PbI₂ films via spin-coating followed by crystallization at temperatures of 100 °C. The 500 nm-thick crystallized MAPbI₃ perovskite thin films showed a Curie temperature of ~ 328 K, a dielectric permittivity of ~ 52, a dielectric loss of ~ 0.02 at 1 MHz, and a low leakage current density of ~ 10⁻⁷ A/cm² at ± 3V. The Polarization-Electric field (*P-E*) hysteresis loop and piezoresponse force microscopy (PFM) results showed that the films had well-developed ferroelectric properties and switchable polarization. Poling at an electrical field of 80 kV/cm enhanced the power density of the generator. The values for output voltage and current density of the poled films reached 2.7 V and 140 nA cm⁻², respectively, which was 2.7-fold higher than those of the non-poled samples.

Introduction

Recently, $\text{CH}_3\text{NH}_3\text{PbX}_3$ perovskite ($X = \text{Cl, Pb, I}$) with a direct band gap energy of 1.5~2 eV has shown outstanding properties as an absorber layer in perovskite solar cells, with an increase from 3.8% to more than 19.3% in only 4 years, and has been identified as a possible base material for high-efficiency commercial photovoltaics.¹⁻⁶ High power-conversion efficiencies using MAPbI_3 have been achieved in both mesoporous structures and planar heterojunction structure devices, using either spin-coating or thermal-evaporation deposition methods.⁷⁻¹⁰ However, the use of solar energy has both time- and location-dependent characteristics that can present problems, such as the recent abrupt changes in the weather caused by the El Nino phenomena that can reduce the power produced by solar cells.

Energy harvesting from the ambient environment and biomechanical movement have attracted interest in wearable and sustainable technologies. Although the energy output by piezoelectric generators may not be as large as that from solar energy, these also have their own advantages such as independence from natural conditions, universality, and flexible characteristics. These advantages make them useful as an energy supply for microelectronic systems and wearable electronic devices.

MAPbI_3 has a cubic perovskite structure at high temperature, which undergoes a cubic-tetragonal transition as the temperature decreases.^{11,12} The ferroelectric polarizations caused by these types of structural characteristics have been thoroughly investigated by various researchers.¹³⁻¹⁵ The polarization switching and light-enhanced piezoelectricity of MAPbI_3 materials has also been addressed by Coll et al.¹⁶ However, to the best of our knowledge, no study has reported the piezoelectric energy harvesting devices using MAPbI_3 perovskite thin films. Thus, both piezoelectric and photovoltaic energy harvesting can be achieved in a single

device by using the same materials, enabling energy harvest irrespective of time and/or environmental variations. Therefore, MAPbI₃ perovskites can potentially be adopted for realizing hybrid energy harvesting devices. In this study, structural and ferroelectric properties of 500 nm-thick MAPbI₃ thin films were investigated in detail and adopted to demonstrate the performance of piezoelectric generators.

Results and discussion

Figure 1 (a) shows X-ray diffraction (XRD) patterns measured at room temperature using MAPbI₃ films annealed at different temperatures. The final thickness of the MAPbI₃ films was approximately 500 nm irrespective of the annealing temperature. The samples annealed under a dry air atmosphere for 3 h from 80 to 130 °C using CH₃NH₃I (MAI) layers deposited onto PbI₂ films showed a well-crystallized MAPbI₃ structure with a polycrystalline nature. However, an extra PbI₂ phase in the samples annealed at 150 °C was observed at XRD $2\theta = 13^\circ$. This result suggested that PbI₂ was formed by a dissociation from MAPbI₃ caused by the evaporation of MAI, which resulted in a thermally unstable state above 130 °C. The MAPbI₃ materials were known to undergo cubic-tetragonal transition to a tetragonal structure at room temperature.^{11,12} In order to investigate the crystal structure of MAPbI₃ at room temperature, the MAPbI₃ thin films were observed at room temperature via high-resolution XRD (HRXRD). Figures 1 (b) and 1 (c) show the HRXRD patterns at $2\theta = \sim 14^\circ$ and $\sim 28^\circ$, respectively. The cubic phase of the MAPbI₃ showed a single peak in the (100) plane at $2\theta = 14^\circ$ and also a single peak in the (200) plane at $2\theta = 28^\circ$.¹⁷ However, as shown in Fig. 1(b), although the peaks near $2\theta = 14^\circ$ were not as well developed, they seemed to be overlapped by those two peaks. Therefore, these were considered to be different peaks, and were noted as peaks in the (002) and (110) planes. As shown in Fig. 1 (c), the peaks observed at near $2\theta =$

28° were clearly separated as $2\theta = 28.3^\circ$ and 28.6° , which indicated the (004) and (220) planes, respectively. Based on the XRD patterns observed at room temperature using the MAPbI₃ films annealed at 100 °C for 1 h under an air atmosphere, the MAPbI₃ films showed a tetragonal structure at room temperature, which was consistent with the results reported in the previous work.¹⁷ Figure 1 (d) shows the scanning electron microscopy (SEM) surface image of the MAPbI₃ films annealed at 100 °C for 3 h under an air atmosphere. The dense and uniform grains were well developed with a mean grain size of approximately 603 nm. On the other hand, as shown in the inset of Fig. 1 (d), samples annealed at 100 °C for 1 h showed disparate grain morphologies that were composed of small grains (mean grain size of approximately 170 nm). This result suggested that the grain morphologies of the MAPbI₃ films were critically dependent on annealing time at 100 °C. The XRD patterns of the MAPbI₃ films annealed at 100 °C up to 4h (Fig. S1, Supplementary information) showed no evolution of the PbI₂ phase.

The Curie temperature using samples annealed at 100 °C for 1h was investigated for the ferroelectric properties of the MAPbI₃ films at room temperature. First, high-temperature XRD was used for the investigation of the transitions in the cubic-tetragonal structure of the MAPbI₃ films as a function of temperature. Figure 2 (a) shows the variations in XRD patterns observed *in situ* at near $2\theta = 28^\circ$ with increasing temperature using high-temperature XRD. Because the peaks at $2\theta = 28^\circ$ were clearly separated at room temperature, the cubic-tetragonal transitions could be studied. As shown in Fig. 2 (a), the XRD (004) peak disappeared slightly with increasing temperature and it had completely disappeared within a temperature range of approximately 56-59 °C. In addition, the XRD (220) peak that indicates the tetragonal structure was changed to a cubic (200) peak when the temperature was

increased above 56 °C. Based on the XRD patterns observed at different temperatures, the Curie temperature of the MAPbI₃ films ranged from 56-59°. To observe the Curie temperature that would be exhibited during a dielectric transition, the dielectric permittivity of the MAPbI₃ films was plotted with temperature, as shown in Fig. 2(b). The Curie temperature of MAPbI₃ films is reported to occur from 327-330 K.^{11,12,18} The dielectric permittivity increased with temperature increases from 298 to 328 K and then decreased with temperature increases above 328 K. This result suggested that the Curie temperature of the MAPbI₃ films was approximately 328 K, which is consistent with the reported results.

Because the MAPbI₃ films prepared via a single-step spin-coating process using MAPbI₃ solutions showed neither dense nor uniform morphologies, they were deposited via a two-step process. After the deposition of PbI₂ onto the FTO/glass, both low- and high-concentrate MAI solutions were spin-coated onto the PbI₂ films, and subsequently they were annealed to form the MAPbI₃ films.¹⁹ In this two-step process, it was important to determine the existence of the Pb element in the surface of the 500 nm-thick MAPbI₃ films for homogeneous compositional distribution. Figure 2 (c) shows the elemental distribution of Pb and I in the MAPbI₃ films, and Sn and F in the FTO electrode along the depth of the 500 nm-thick MAPbI₃/FTO substrate. Based on the SIMS profile, Pb and I elements were clearly distributed on the film surface. However, the Pb and I elements were remarkably diffused into the FTO, although the annealing temperature was as low as 100 °C. In order to investigate the origin of the remarkable diffusion of the Pb and I elements, elemental mapping via SIMS was performed, and the results are shown in Fig. 2 (d). Where the Pb elements are highlighted in green in the MAPbI₃ films, and the F elements are highlighted in blue in the FTO electrode. The mapping image shows the Pb element within the FTO layer.

However, when the rms roughness of the FTO was as high as 20 nm, the inhomogeneous distribution of the Pb elements in the interface between the MAPbI₃ films and the FTO was attributed to the high roughness of the FTO electrode. Auger electron spectroscopy depth-profile was performed to identify the homogeneous distribution of the Pb⁺² and I⁻¹ elements using the MAPbI₃ films deposited onto the Au/Ti/glass, and the results are shown in Fig. S2 (Supplementary information).

For transparent characteristics of the 500 nm-thick MAPbI₃ films, absorption spectra of the films as-deposited onto the FTO/glass and annealed at 100 °C for 1h were shown in Fig. S3 (Supplementary information). The colors of the annealed MAPbI₃ films were not varied as a transparent dark-brown, as-compared with that of as-deposited samples. Based on the absorption spectra, high absorptions in the range of 300 to 500 nm wavelength were observed, and then they rapidly decreased with increasing wavelength above 500 nm. The absorption spectra of the samples before and after annealing showed similar tendencies with increasing wavelength.

The dielectric and the leakage properties of the 500 nm-thick MAPbI₃ films annealed at 100 °C for 1h are shown in Figs. 3 (a) and 3 (b), respectively. As shown in Fig. 3 (a), the crystallized films at 100 °C showed an approximate dielectric permittivity of 52 and a dielectric loss of 0.02 at 1 MHz, which indicated a high dielectric constant in the crystallized thin films annealed at a low temperature. The leakage current density in dielectric materials should be low because the electric field was applied to align the dipoles in order to enhance the dielectric properties of the thin films. Figure 3 (b) shows the leakage current density vs. applied voltage of the MAPbI₃ films. The leakage properties of the films were as low as $\sim 10^{-7}$ A/cm² in the range of ± 3 V because the marginal leakage current density in the dielectric films was approximately below 1 μ A/cm² at an optional applied voltage. The breakdown

strength of the 500 nm-thick MAPbI₃ films was approximately 60 kV/cm. The polarization hysteresis loops were observed to investigate the ferroelectric properties of the MAPbI₃ films. Figure 3 (c) shows the relationship between the polarization and applied voltage of the MAPbI₃ films annealed at 100 °C for 1h. Although the P-E curves were not fully saturated at an applied voltage of $\pm 3V$, the hysteric behavior of the P-E curves was observed. This indicated switchable ferroelectric polarizations in the MAPbI₃ films, and showed that the values for remnant polarization (P_r) and the coercive field ($2E_c$) were 0.15 $\mu\text{C}/\text{cm}^2$ and 36 kV/cm, respectively.

In order to investigate the local polarization state of the MAPbI₃ films annealed at 100 °C for 1h, PFM analysis was performed. Fig. 3 (d) shows the topography of the MAPbI₃ films annealed for 1h. The grains were small, approximately 170 nm, due to short annealing time (see Fig. S4 (Supplementary information)). The PFM amplitude and phase images, which were simultaneously obtained with the topography (Fig. 3 (d)), are shown in Figs. 3 (e), and 3 (f), respectively. The obtained PFM phase image and corresponding histogram (inset in Fig. 3 (f)) clearly indicated that the MAPbI₃ films had a preferred polarization direction. We further explored the local ferroelectric properties using piezoresponse hysteresis loops. Since the averaged amplitude and phase hysteresis loops showed typical butterfly and rectangular shapes (Figs. 3 (g) and (h), respectively), the results confirmed the existence of ferroelectricity in the MAPbI₃ films even on a nanoscale. The piezoresponse hysteresis loop also reflected this tendency, as shown in Fig. 3 (i). Since ferroelectric materials also possess piezoelectricity, the results show that MAPbI₃ films can be utilized for energy-harvesting applications. Thus, to explore piezoelectric properties, the d_{33} piezoelectric coefficient of the MAPbI₃ films was gauged by measuring the V_{ac} -dependent piezoresponses. As shown in Fig. S5 (Supplementary information), the measured piezoelectric coefficient was approximately

5.12 pm/V, which was similar to values reported in previous reports.²⁰

To demonstrate the application of MAPbI₃ to piezoelectric generators, thin-film piezoelectric generators using 500 nm-thick MAPbI₃ thin films annealed at 100 °C for 1h were fabricated. Specifically, two substrates, PET/indium-tin oxide (ITO) and MAPbI₃/Au/Ti/PET, were combined using Polydimethylsiloxane (PDMS) as an adhesive layer to sandwich an active piezoelectric layer between two electrode layers. The details of the fabrication process can be found in the Methods section, and the real photograph of energy harvesting device and measurement setup were shown in Fig. S6 (Supplementary information). Here, two devices were prepared for piezoelectric output performance measurement: an as-fabricated device [Fig. 4 (a)] and a device poled under a high electric field (80 kV/cm) [Fig. 4 (b)]. The power generation mechanism of two MAPbI₃ piezoelectric thin film generators is schematically described in Figs. 4 (a) and 4 (b). When the device was pushed, a piezoelectric potential was induced in the MAPbI₃ piezoelectric film, forcing electrons to move toward the top electrode through an external circuit until accumulated electrons balance the piezoelectric potential, generating a positive voltage and a current pulse. As the pressure was released, the induced piezoelectric potential in the MAPbI₃ rapidly vanished and the accumulated electrons on the top electrode flowed back to the bottom electrode, generating negative voltage/current pulses. In this application, the PDMS layer served as a potential barrier for electrons, preventing internal leakage of the current between the two electrodes through the active piezoelectric layer. In a non-poled device [Figure 4 (a)], the polarization domain of the MAPbI₃ piezoelectric film is randomized at its initial state. Thus, when pressure is applied, the generated net piezoelectric potential is relatively small. When the piezoelectric generator [Fig. 4 (b)] was poled under a high electric field, however, it exhibited a much higher piezoelectric potential compared with that of the non-poled

piezoelectric generator. Values for the output voltage and current of the fabricated devices generated by periodically applied pressure are shown in Figs. 4 (c) and 4 (d), respectively, for non-poled devices. During this measurement, a 10 M Ω load resistance was connected, and what is considered to be a normal constant pressure of 0.5 MPa was periodically applied to a 1 cm² area of the generator. The non-poled device generated a peak voltage and current of 1.0 V and 50 nA cm⁻², respectively. In device poled at 80 kV/cm [Fig. 4 (e) and 4 (f)], however, the values for voltage and current were increased to 2.7 V and 140 nA cm⁻², respectively, which averaged a 2.7-fold increase by comparison with those of the non-poled samples. The output performance of the MAPbI₃ piezoelectric generator was comparable to that (peak voltage and current of 6.5 V and 70 nA cm⁻², respectively) of the BaTiO₃ film-based piezoelectric generator, as reported by Gao et al.²¹ This result clearly indicated that the domain alignment of the MAPbI₃ thin film layer played an important role in enhancing the performance of the piezoelectric generators.

Figure 5 (a) showed variations in peak voltage and current density of the generators as a function of poling electric field. During the measurement, the applied pressure was maintained at 0.5 MPa. The peak output voltages and current densities of the generators were linearly increased with increasing poling electrical field by 80 kV/cm, and then they were saturated at 100 kV/cm. Dielectric breakdown was occurred at poling fields of above 100 kV/cm. The peak output voltage and current density of the piezoelectric generators after poling at 80 kV/cm were measured under various applied forces and the result was shown in Fig. 5 (b). The peak output voltages and current densities were linearly increased with the applied force from 0.1 to 0.3 MPa and then they were slight saturated at applied forces from 0.3 MPa. The highest output voltage and current density of the MAPbI₃ piezoelectric generators are approximately 2.7 V and 140 nA/cm², respectively at poling field of 80 kV/cm

and applied force of 0.5 MPa. The piezoelectric potential generated in the MAPbI₃ perovskite thin films was also calculated using COMSOL Multiphysics® software and their result were shown in Fig. S7 (Supplementary information). Approximately 3 V of piezoelectric potential difference was developed across MAPbI₃ perovskite thin film, which is similar to the values experimentally measured. Next, validity of output voltage and current was also confirmed by switching polarity test, measuring the output signals in a reverse connection mode. The measured output signals in Figs. 5 (c) and 5 (d) are exactly reversed in comparison with the values measured in a forward connection mode [Fig. 4(e), 4(f)]. These results confirmed that the measured output signals were indeed generated by the piezoelectric generator.

Conclusions

MAPbI₃ perovskite thin films were applied to FTO/glass and Au/Ti/PET substrates via a two-step process, which involved depositing a MAI solution onto PbI₂ films via spin-coating followed by crystallization at temperatures of 100 °C. Curie temperature, exhibiting a transition from cubic to tetragonal structure of MAPbI₃ thin films, was observed at ~ 328 K as indicated by both high-temperature XRD and relationship between dielectric constant and temperature. The P-E hysteresis loop and PFM results showed that the films had well-developed ferroelectric properties and switchable polarization. Poling at an electric field of 80 kV/cm enhanced the power density of the piezoelectric generator. The output voltage and current density of the poled films reached 2.7 V and 140 nA cm⁻², respectively, which was 2.7-fold higher than those measured from the non-poled samples. This innovative approach could be helpful for potential applications in hybrid energy harvesting devices and wearable energy harvesting devices.

Methods

Applying MAPbI₃ thin film onto a FTO-coated glass substrate

A PbI₂ solution was prepared at 60 °C using PbI₂ (0.04g) and N, N-Dimethylformamide (HCON(CH₃)₂) (~ ml). The PbI₂ solution was spin-coated at 4,000 rpm for 40 s onto a FTO-coated glass substrate accompanied by the flowing of air at 60 °C onto the substrate during deposition in order to maintain a high temperature. Here, the thickness of the PbI₂ films was approximately 800 nm. When the substrate temperature fell below that of the PbI₂ solution during deposition, the deposited PbI₂ became opaque. The deposited PbI₂ became transparent because the solvent in the PbI₂ solution was rapidly evaporated by the flow of hot air during deposition. MAI solutions were deposited onto the PbI₂-coated FTO-glass substrate using spin coating via a two-step process. First, a low-concentrate-MAI solution (2 mg/1 ml) was spin-coated at 2,000 rpm for 5 s onto the PbI₂-coated FTO glass in order to promote uniform film growth. Second, a high-concentrate-MAI solution (40 mg/1 ml) was dropped onto the low-concentrate-MAI layer and was maintained for 3-4 minutes to stabilize the wetting of the low-concentrate-MAI layer. The samples were maintained at 2,000 rpm for 20 s. After the spin-coating of the low- and high-concentrate-MAI layers, the MAPbI₃ films were prepared via annealing at different temperatures at various durations under a dry air atmosphere.

Characterization and electrical properties of the MAPbI₃ piezoelectric films

The crystallinity and the morphologies of the MAPbI₃ films were characterized via XRD and SEM, respectively. The phase changes of the MAPbI₃ films were investigated via high-temperature XRD under different temperatures. The elemental distribution and mapping image of the Pb⁺² and I⁻¹ in the MAPbI₃ films deposited onto the FTO electrode was studied

via secondary ion mass spectroscopy (SIMS). The elemental distribution of the MAPbI₃ films deposited onto the Au/Ti/glass substrate was also investigated via Auger electron spectroscopy (AES). The dielectric and leakage properties of the MAPbI₃ films were measured using an Au/MAPbI₃/FTO/glass (metal-insulator-metal) structure using HP4194A impedance gain-phase and HP4194B semiconductor-parameter analyzers, respectively. Values for the area and thickness of the Au top electrode were $100 \times 100 \mu\text{m}^2$ and 200 nm, respectively. The polarization-voltage hysteresis curve of the ferroelectric MAPbI₃ was determined using an RT 66A ferroelectric tester (Radiant Technology) operated in virtual ground mode.

The PFM measurements were conducted using a commercial atomic force microscope (NX-10, Park Systems) with a Pt-coated conductive cantilever (Multi75E-G, BudgetSensors). To acquire the PFM images, an ac modulation voltage of $1.5 V_{rms}$ and 17 kHz was applied to the conductive tip using a lock-in amplifier (SR830, Stanford Research Systems). The piezoelectric coefficient, d_{33} , was obtained using a general V_{ac} sweep method.^{22,23} Here, the ac modulation voltage was progressively increased from $0 V_{rms}$ to $3 V_{rms}$ with 17 kHz applied at the tip. The piezoresponse hysteresis loops were obtained using a band excitation (BE) technique.²⁴ To utilize the BE technique, a function generator (PXIe-1062Q, National Instruments) was connected with PFM. Pulses ranging from -9 to 9 V_{dc} with a 1 V_{pp} BE waveform at 230-310 kHz were applied to measure the piezoresponse hysteresis loop.

Energy harvesting using the MAPbI₃ films

(1) Device fabrication

PDMS was spin-coated onto the ITO-deposited PET substrate at 3500 rpm for 30 s. The PDMS layer was 25 μm thick. The PDMS-coated electrode layer was then combined with a prepared active ferroelectric dye layer on an Au (400 nm)/Ti (10 nm)/PET substrate, which was then cured in an oven at 95 $^{\circ}\text{C}$ for 3 h. Finally, the fabricated devices were poled in order to align the polarization domain of the active layer while applying various electric fields at room temperature.

(2) Device characterization

The output performances of the piezoelectric generator were characterized using a low-noise current amplifier (SR 570, Stanford Research Systems) and an oscilloscope (LT 354, Lecroy Waverunner) with a 10 Mega Ohm load resistance. During measurement, a periodic force (0.5 MPa) was applied normal to the device surface using a custom-built pushing machine at 0.5 Hz. The active sample area under the stress measured 1 cm \times 1 cm.

References

1. Kojima, A., Teshima, K., Shirai, Y., Miyasaka, T. Organometal halide perovskites as visible-light sensitizers for photovoltaic cells. *J. Am. Chem. Soc.* **131**, 6050 (2009).
2. Lee, M., Teuscher, J., Miyasaka, T., Murakami, T., Snaith, H. Efficient Hybrid Solar Cells Based on Meso-Superstructured Organometal Halide Perovskites. *Science*. **338**, 643 (2012).
3. Snaith, H. J., Perovskites: The Emergence of a New Era for Low-Cost, High-Efficiency Solar Cells. *J. Phys. Chem. Lett.* **4**, 3623 (2013).
4. Jeon, N. J., Noh, J., Kim, Y., Yang, W., Seo, J., Seok, S. Compositional engineering of perovskite materials for high-performance solar cells. *Nat. Mater.* **13**, 897 (2014).

5. Donald, R. O., Stephen P. L., Limits on Yields in the Corn Belt. *Science*. **344**, 485, 6183 (2014).
6. Noh, J., Im, S., Heo, J., Mandal, T. & Seok, S. I. Chemical Management for Colorful, Efficient, and Stable Inorganic–Organic Hybrid Nanostructured Solar Cells. *Nano Lett.* **13**, 1764 (2013).
7. Mingzhen Liu., Michael, B., Johnston & Henry, J., Snaith. Efficient planar heterojunction perovskite solar cells by vapour deposition. *Nature*. **501**, 395 (2013).
8. Xiao, Z., Dong, Q., Bi, C., Shao, Y., Yuan, Y., Huang., Solvent Annealing of Perovskite-Induced Crystal Growth for Photovoltaic-Device Efficiency Enhancement. *J. Adv. Mater.* **26**. 6503 (2014)
9. Heo, J. H., Im, S. H., Noh, J. H., Mandal, T. N., Lim, C. –S., Chang, J. A., Lee, Y. H. Kim, H. –J., Sarkar, A., Nazeeruddin, M. K., Efficient inorganic-organic hybrid heterojunction solar cells containing perovskite compound and polymeric hole conductors. *Nat. Photonics*. **7**, 486 (2013).
10. Docampo, P., Ball, J. M., Darwich, M., Eperon, G. E., Snaith, H. J. Efficient organometal trihalide perovskite planar-heterojunction solar cells on flexible polymer substrates. *Nat. Commun.* **4**, 2761 (2013).
11. Weber, D., $\text{CH}_3\text{NH}_3\text{PbX}_3$, a Pb(II)-System with Cubic Perovskite Structure. *Z. Naturforsch.* **33b**, 1443 (1978).
12. Poglitsch A.; Weber D. Dynamic Disorder in Methylammonium trihalogenoplumbates (II) Observed by Millimeter-wave Spectroscopy. *J. Chem. Phys.* **87**, 6373–6378 (1987).

13. Frost, J. M., Butler, K. T. Brivio, F., Hendon, C. H. van Schilfgaarde, M., Walsh, A., Atomistic origins of high-performance in hybrid halide perovskite solar cells. *Nano Lett.* **14**, 2584 (2014).
14. Frost, J. M., Butler, K. T., Walsh, A. Molecular ferroelectric contributions to anomalous hysteresis in hybrid perovskite solar cells. *APL Mater.* **2**, 081506 (2014).
15. Liu, S., Zheng, F., Koocher, N. Z., Takenaka, H., Wang, F., Rappe, A. M. Ferroelectric Domain Wall Induced Band Gap Reduction and Charge Separation in Organometal Halide Perovskites. *J. Phys. Chem. Lett.* **6**, 693 (2015).
16. Coll, M., Gomez, A., Marza, E. M., Almora, O., Belmonte, G. G., Quiles, M. C. and Bisquert, J. Polarization Switching and Light-Enhanced Piezoelectricity in Lead Halide Perovskites. *J. Phys. Chem. Lett.* **6**, 1408 (2015).
17. Oku, T., Zushi, M., Imanishi, Y., Suzuki, A. and Suzuki, K. Microstructures and photovoltaic properties of perovskite-type $\text{CH}_3\text{NH}_3\text{PbI}_3$ compounds. *Appl. Phys. Express.* **7**, 121601 (2014).
18. Yamamuro, N. O., Matsuo, T. and Suga, H. Calorimetric and IR spectroscopic studies fo phase transitions in methy-lammonium trihalogenoplumbates (II). *J. Phys. Soc. Solids.* **51**, 1383 (1990).
19. Kim, Y. J., Tung, D. T., Choi, H. J., Park, B. J., Eom, J. H., Kim, K. S., Jeong, J. R. and Yoon, S. G. Enhanced reproducibility of the high efficiency perovskite solar cells via a thermal treatment. *RSC Advances.* **5**, 52571 (2015).
20. Kim, H. S., Kim, S. K., Kim, B. J., Shin, K. S., Gupta, M. K., Jung, H. S., Kim, S. W. and Park, N. G. Ferroelectric Polarization in $\text{CH}_3\text{NH}_3\text{PbI}_3$ Perovskite. *J. Mater. Chem. A.* **3**, 20352-20358 (2015)

21. T. Gao, J. Liao, J. Wang, Y. Qiu, Q. Yang, M. Zhang, Y. Zhao, L. Qin, H. Xue, Z. Xiong, L. Chen, and Q. M. Wang, *J. Mater. Chem. A*, **3**, 9965 (2015).
22. Kim, Y. S., Alexe, M. and Ekhard K. H. Salje. Nanoscale properties of thin twin walls and surface layers in piezoelectric WO_{3-x} . *Appl. Phys. Lett.* **96**, 032904 (2010).
23. Seol, D. H., Seo, H. S., Stephen, J., Kim, Y. S. Nanoscale mapping of electromechanical response in ionic conductive ceramics with piezoelectric inclusions. *J. Appl. Phys.* **118**, 072014 (2015).
24. Stephen, J., Sergei V.K. Band excitation in scanning probe microscopy: sines of change. *J. Phys. D: Appl. Phys.* **44**, 464006 (2011)

Acknowledgements

This work was supported by a National Research Foundation of Korea (NRF) grant funded by the Korea government (MSIP) (No. NRF-2015R1A2A1A01003867)

Figure captions

Fig. 1 (a) XRD patterns measured at room temperature using the $MAPbI_3$ films annealed at different temperatures. Enlarged XRD patterns at 2θ of (b) $\sim 14^\circ$ and (c) $\sim 28^\circ$. (d) SEM surface image of the $MAPbI_3$ films annealed at 100°C for 3 h under an air atmosphere. Inset of (d) showed the SEM image of the films annealed at 100°C for 1 h.

Fig. 2 (a) Variations in XRD patterns observed *in situ* at near $2\theta = 28^\circ$ with increasing temperature using a high-temperature XRD. (b) Relationship between dielectric

permittivity and temperature for the clear observation of the MAPbI₃ Curie temperature. Here, heating rate for the observation of the dielectric permittivity with increasing temperature was approximately 2° min⁻¹. (c) SIMS elemental distribution of Pb and I observed along the depth of MAPbI₃ films. (d) SIMS mapping image of the Pb and I of the MAPbI₃ films deposited onto the high-roughened FTO bottom electrode.

Fig. 3 (a) Variations in dielectric permittivity and dissipation factor of the MAPbI₃ films as a function of frequency. (b) Leakage current density vs. applied voltage of the 500 nm-thick MAPbI₃ films. (c) P-E hysteresis loop of the 500 nm-thick MAPbI₃ films. (d), (e), and (f) PFM topography, amplitude, and phase images, respectively. Image size is 3 μm × 3 μm. (g), (h), and (i) Piezo amplitude, Piezo-phase hysteresis loops, and Piezo-response of the MAPbI₃ films recorded at a scan rate of 0.5 Hz, respectively.

Fig. 4 (a), (b) The power generation mechanisms of MAPbI₃ piezoelectric thin film generators under non-poled and poled conditions, respectively. (c), (d) Open-circuit voltage outputs and short-circuit current density outputs of the non-poled piezoelectric generator measured in a forward connection mode, respectively. (e), (f) Open-circuit voltage outputs and closed-circuit current density of the piezoelectric generator poled at 80 kV/cm, respectively.

Fig. 5 (a) Variations in peak output voltage and current density for different poling fields at an applied pressure of 0.5 MPa. (b) Relationship between peak voltages and current densities as a function of applied pressure for piezoelectric generators poled at 80 kV/cm. (c) Open-circuit voltage outputs and (d) short-circuit current density of the

piezoelectric generator poled at 80 kV/cm measured in a reverse connection mode.

Applied pressure was maintained at 0.5 MPa.

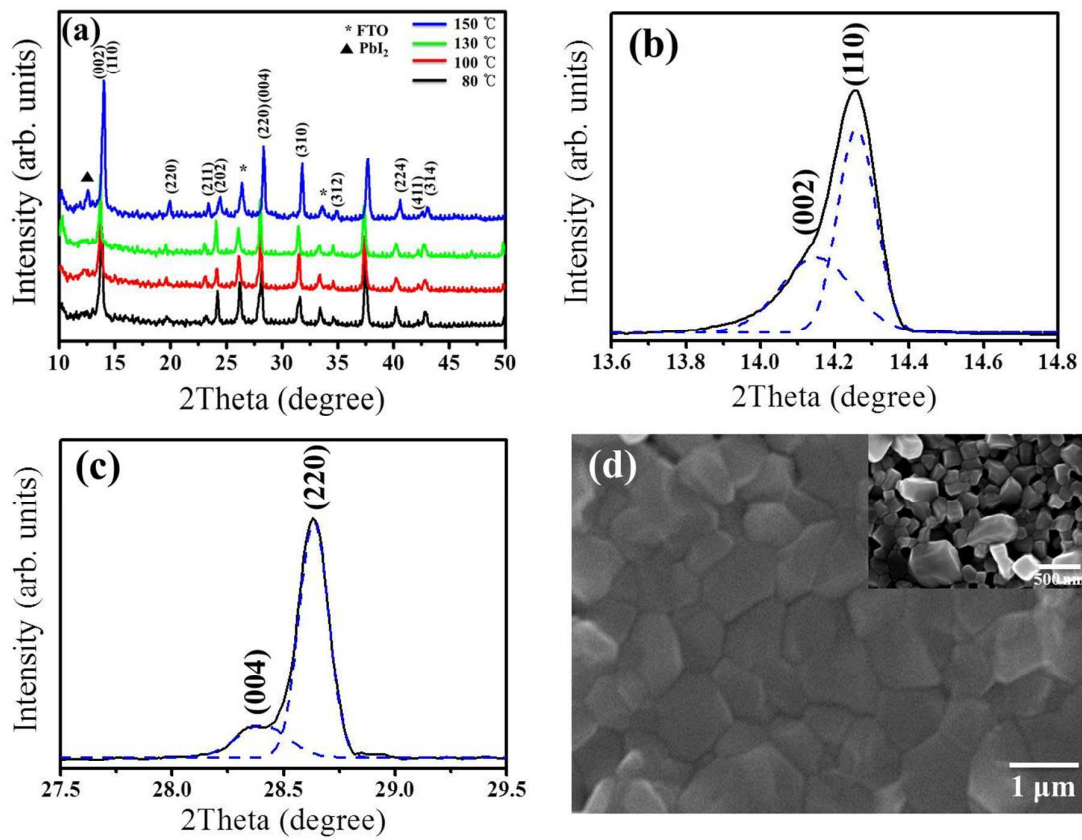


Fig. 1

Y. J. Kim et. al

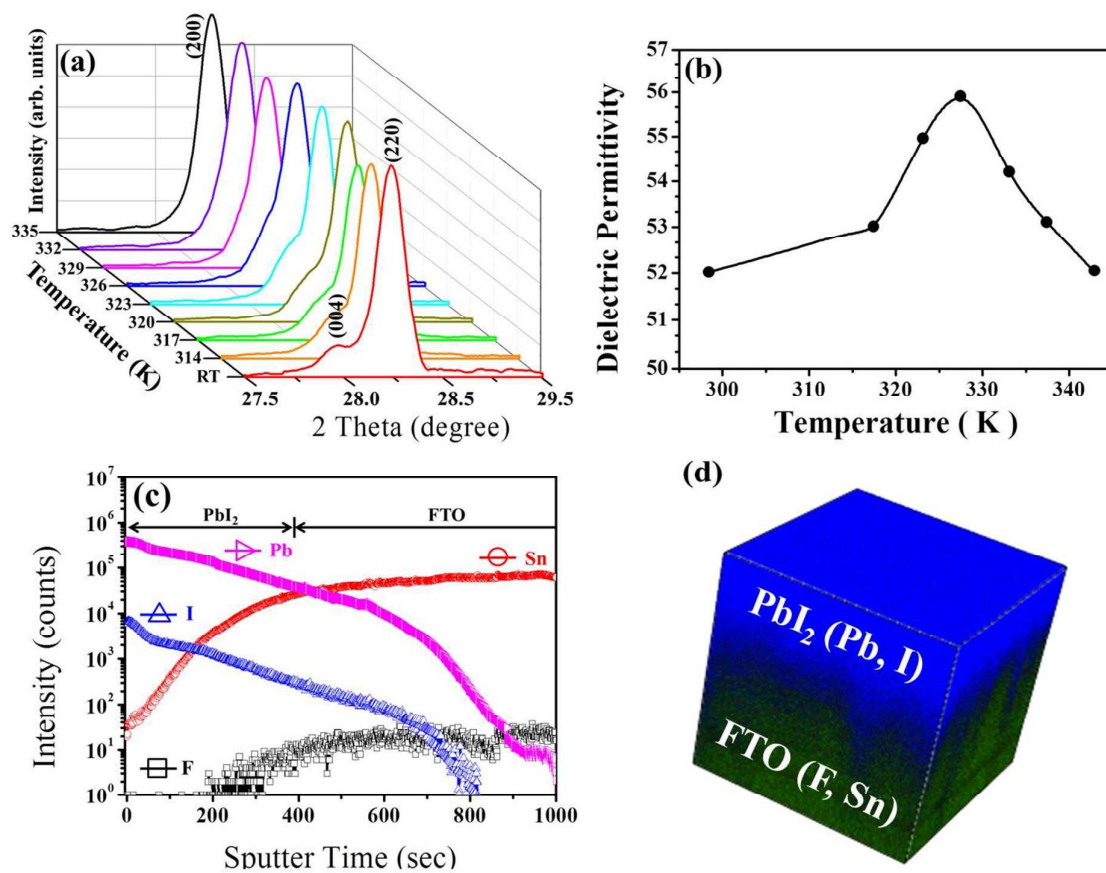


Fig. 2

Y. J. Kim et. al

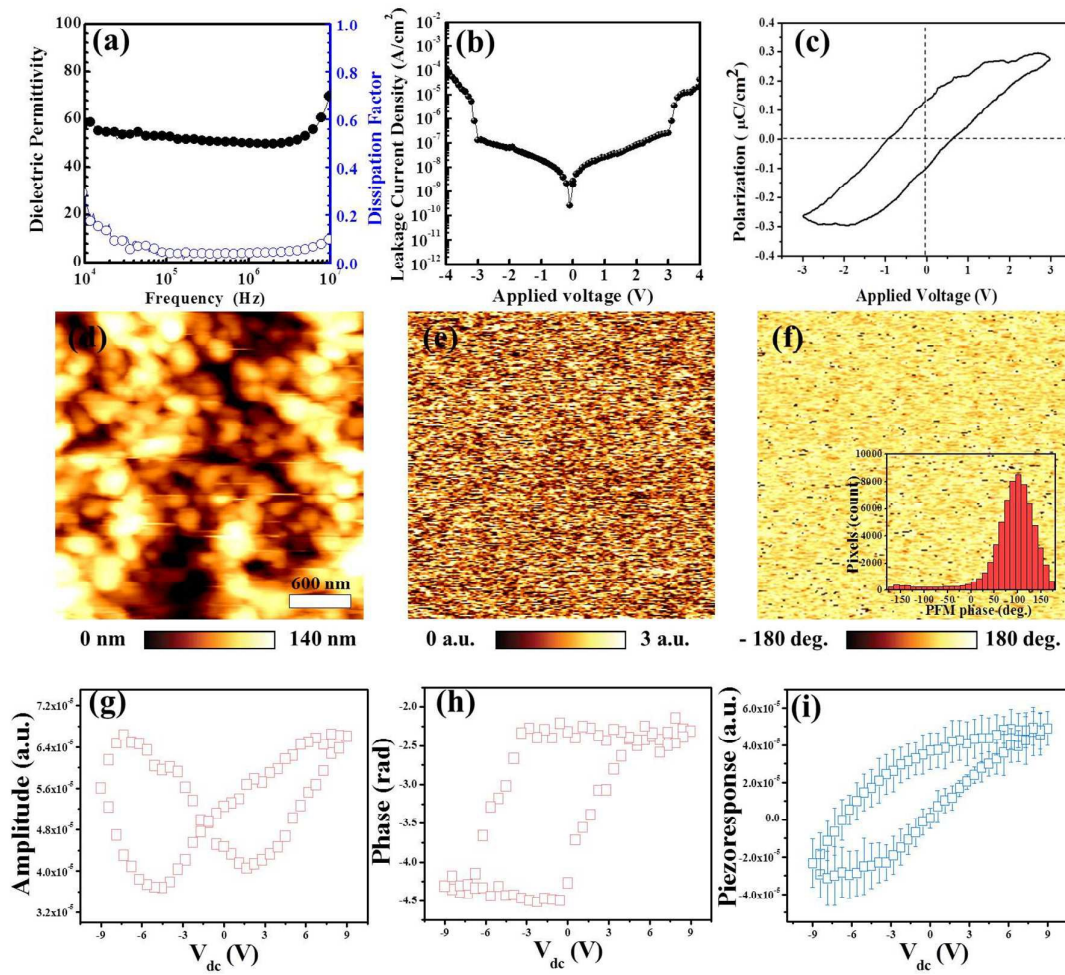


Fig. 3

Y. J. Kim et al

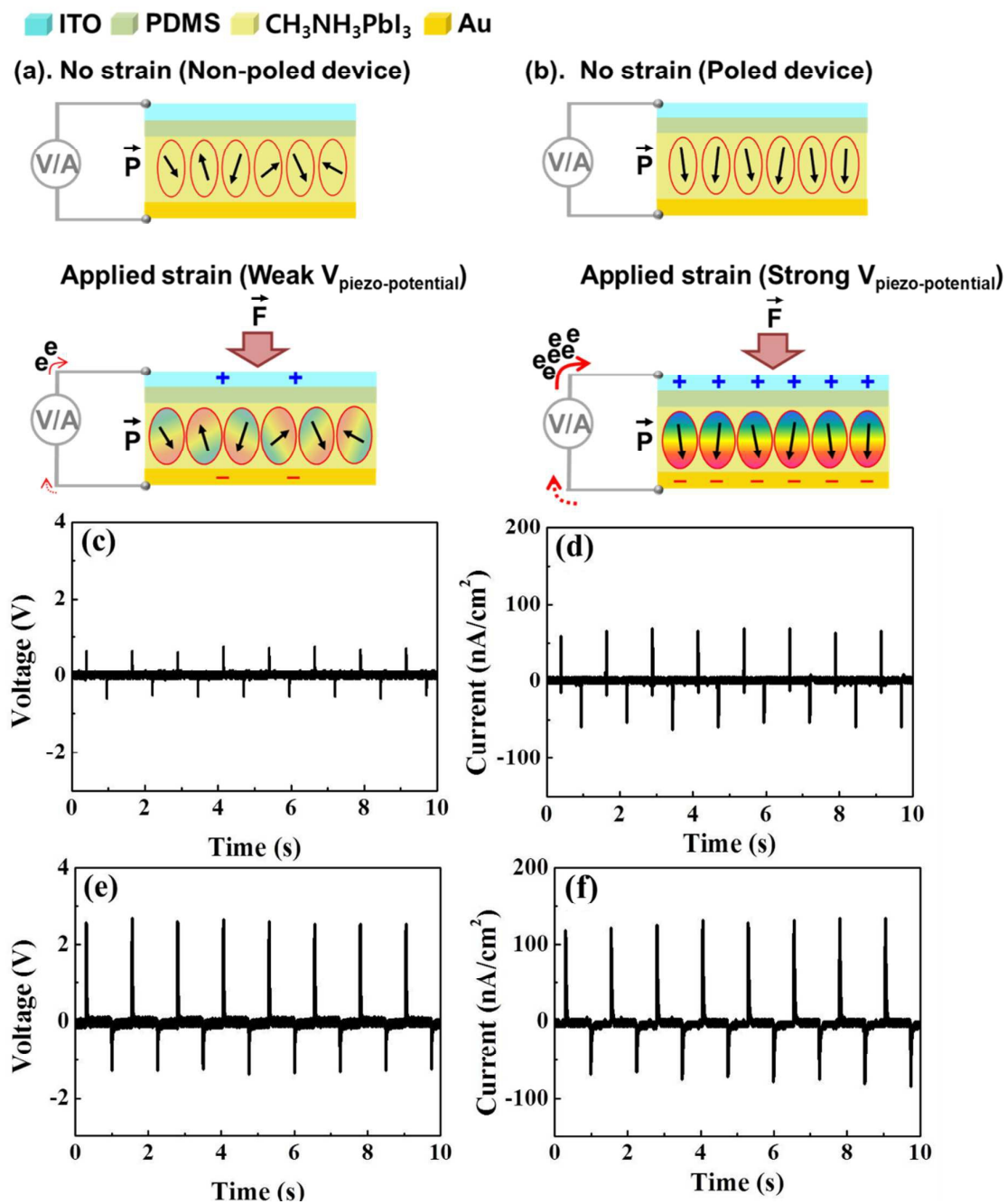
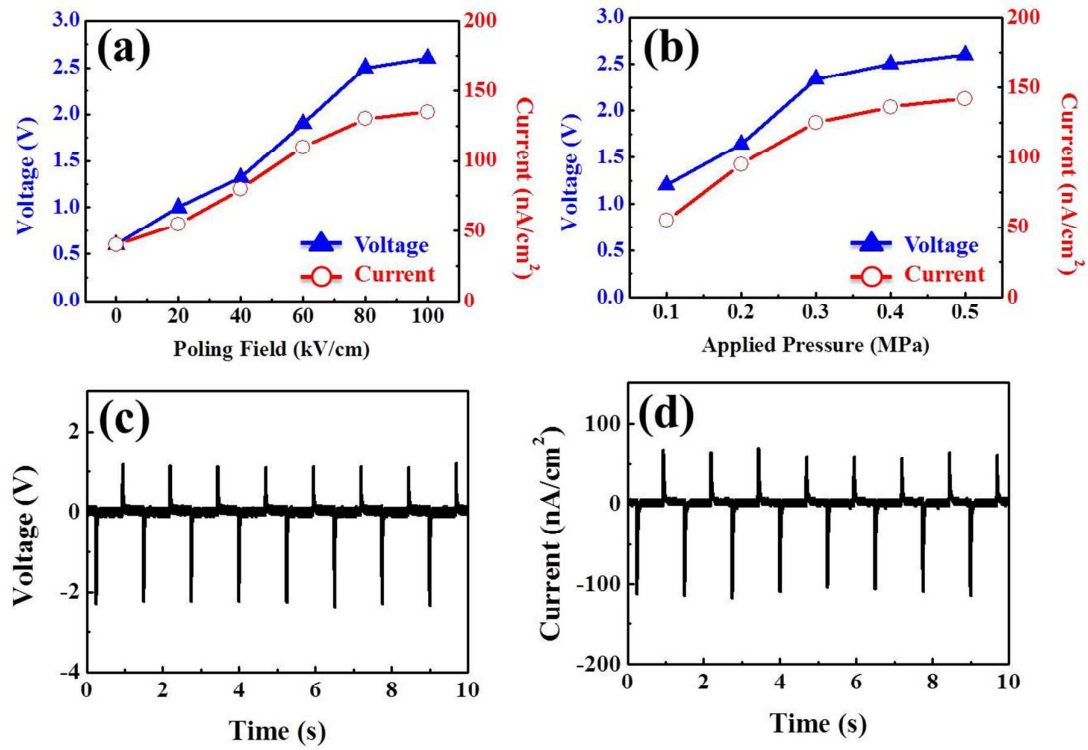


Fig. 4

Y. J. Kim et. al

**Fig. 5***Y. J. Kim et. al*